LES study of diesel flame/wall interaction and mixing mechanisms at different wall distances

Pucilowski, Mateusz; Jangi, Mehdi; Fatehi, Hesameddin; Pang, Kar Mun; Bai, Xue-song

DOI:
10.1016/j.proci.2020.05.056

Document Version
Peer reviewed version

Citation for published version (Harvard):
Pucilowski, M, Jangi, M, Fatehi, H, Pang, KM & Bai, X 2021, 'LES study of diesel flame/wall interaction and mixing mechanisms at different wall distances', *Proceedings of the Combustion Institute*, vol. 38, no. 4, pp. 5597-5604. https://doi.org/10.1016/j.proci.2020.05.056

LES study of diesel spray/wall interaction and mixing mechanisms at different wall distances

Mateusz Pucilowski[a,*], Mehdi Jangi[b], Hessameddin Fatehi[a], Kar Mun Pang[c], Xue-Song Bai[a]

[a]*Department of Energy Sciences, Lund University, 22100 Lund, Sweden*
[b]*Department of Mechanical Engineering, University of Birmingham, B15 2TT Birmingham, United Kingdom*
[c]*MAN Energy Solutions, 2450 Copenhagen, Denmark*

Abstract

In this paper, the spray-wall interaction of reacting diesel spray under engine like conditions is investigated using large eddy simulations. The aim of this study is to understand the influence of the distance between the wall and the spray nozzle on the air entrainment rate, which is the key variable in the formation/oxidation process of soot. Three experimental cases are investigated, a free jet case and two wall impingement cases with a distance from the nozzle to the wall of 30 mm and 50 mm. The optical soot measurements imply a positive influence of the wall on the rate of soot oxidation. Numerical simulations are employed to elucidate the importance of different mechanisms for the air entrainment, i.e., the mechanism of air entrainment prior to flame lift-off position, the mechanism of enhanced mixing due to the wall impingement, and the mechanism of enhanced mixing by the entrainment wave. The results show that the oxidation process after the end of injection is driven by a different mixing mechanism depending on the

*Corresponding author.
E-mail address: mateusz.pucilowski@energy.lth.se

distance to the wall. The 30 mm case resulted in a "mixing boost", where the dominant mixing mechanism is the wall impingement vortex mixing, which gives rise to the fastest soot decay among the cases. The mixing in the 50 mm case is governed by a late wall impingement vortex mixing, giving rise to a low, but a constant air entrainment rate, i.e., a "mixing plateau". The free jet case resulted in mixing governed by the entrainment wave mechanism. Both wall impingement cases have a faster soot oxidation rate compared with the free jet case, but due to a different underlying mixing process. LES is shown to be able to replicate the line-of-sight measurements of natural OH^* chemiluminescence and distribution of soot region from the optical soot diagnostics.
Keywords:
spray-wall interaction, LES, soot oxidation, diesel spray

1. Introduction

Diesel engines have been widely studied during the last two decades in order to lower the emissions of soot, while improving efficiency. Apart from the after-treatment systems, the reduction of soot emissions in diesel engines can be achieved using a number of in-cylinder methods, e.g., high injection pressure, multiple injection strategies, or exhaust gas recirculation (EGR) [1–3]. These techniques can reduce the soot emissions either by improving the mixing process and thus enhancing the soot oxidation, or by altering the combustion temperature and therefore the soot formation. However, the most important mixing mechanism to reduce the soot emission is the spray-wall interaction. In order to carefully study spray-wall interaction, outside of the complex engine environment, researchers devoted several experimental studies in the constant volume chamber

to characterize the effects of the wall impingement on the soot emissions [4–7].

The experiments of Pickett and Lopez [8] showed that wall impingement had a significant effect on the soot emission. Soot was shown to be reduced due to the wall impingement, possibly by the mechanism of wall cooling that reduced the soot formation (T_{wall}= 500 K), or by the enhanced air mixing that increased the soot oxidation. Similar findings were reported by Wang *et al.* [9], who showed that the total soot emission was reduced by the wall impingement. However, for the cases with wall-wetting, the soot emission could not be improved by the spray-wall interaction, compared with the free jet cases.

Li *et al.* [10, 11] carried out experiments on spray-wall interaction with a focus on the effect of the distance between a flat wall (T_{wall}= 873 K) and injector nozzle. It was found that the wall could affect both the formation and oxidation of soot. The soot formation during the injection, for the wall jet cases, was higher than that for the free-jet case. On the other hand, in the later phase of injection, as the wall recirculation vortices were developed, the soot oxidation for the wall jet cases, was also higher, which resulted in a lower total soot emission compared with the free jet case. The results indicate that soot oxidation plays an important role in the final soot emission, which is favorable for the wall jets cases. The underlying mechanisms for the soot formation and oxidation processes are, however, not clear due to the limited information obtainable in the optical experiments [10, 11].

The experiments of Li *et al.* [10, 11] are studied in the present numerical simulations, aiming to quantify the air entrainment rate, which is considered as the key variable for soot emission, due to the different mixing mechanisms which are (a) air mixing in the upstream region of the flame lift-off position, (b) enhanced air mixing due to wall impingement, and (c) enhanced mixing by entrainment wave

[12, 13]. The goal is to understand their role in the formation/oxidation process of soot. Large eddy simulations (LES) are performed with directly coupled finite-rate chemistry based on a partially stirred reactor (PaSR) sub-grid scale (SGS) model. A phenomenological soot model is employed to identify regions of high soot formation [14] in comparison with measurement of soot optical thickness, KL.

2. Numerical method

In LES, the governing equations are derived for the spatially filtered continuity equation, and transport equations for momentum, species mass fraction, enthalpy, and mixture fraction. The SGS stress and transport fluxes are modeled using a one-equation eddy model, based on the transport equation of SGS turbulent kinetic energy. The liquid spray injection is modeled using the well-known Lagrangian particle tracking (LPT) approach. The Ranz-Marshall correlation is used to compute droplet heat transfer with the surrounding gas phase. The evaporation is modeled using Frossling equations. The Huh-Gosman model and Kelvin-Helmholtz (WAVE) model were used for the primary and the secondary breakup, respectively. Further details of the models are given in our previous work [15], where the model constants used here are specified. The injection profile is taken from the Engine Combustion Network (ECN) database. The spray model is shown to be able to replicate the liquid penetration length in the present free jet case, which was measured with the Mie-scattering technique to be about 26 mm [10, 11]. Vapor phase matches the correct time of the wall impingement and radial penetration.

The ignition and combustion process of diesel fuel (JIS#2) used in the ex-

periments is modeled by a 54-species compact skeletal mechanism of Yao *et al.* [16], known as the SK54 mechanism. This mechanism contains 269 elementary reactions and it was previously employed to simulate similar spray flames from the ECN [17]. The liquid fuel properties used in the simulations, which are appropriate for diesel fuel (JIS#2), are based on a mixture of n-decane (70vol.%) and methylnaphthalene (30 vol.%), known as IDEA.

The soot formation and oxidation process is modeled using a phenomenological model based on two transport equations (number density and mass fraction of soot) [14]. Turbulence-chemistry interaction in the SGS is modeled using the PaSR model [18]. This approach is shown to offer reasonable results in the simulation of spray flames. Further validation of the model will be provided in Section 4.1. The integration of the elementary reaction rates is the most time consuming step of the numerical simulation. This step is accelerated with a so-called chemistry coordinated mapping (CCM) algorithm [19], which clusters the CFD cells based on their chemical composition and their thermodynamic state. A low dimensional phase space is built including temperature, mixture fraction, fuel mass fraction, and scalar dissipation rate. The integration of the reaction rates takes place in the phase space, instead in each individual cell, which can speed up the integration of the stiff reaction rates by a factor of 10 [19]. The numerical solver used is OpenFoam 4.1. Both temporal and spatial terms were discretized with implicit second order schemes.

3. Numerical cases

Three cases from the experimental data of Li *et al.* [10, 11] are considered, including two wall jet cases with the wall to nozzle distance of 30 mm (Case I)

and 50 mm (Case II), and a free jet case (Case III). The computational domain is a rectangular box, cf. Fig. 1. Table 1 shows the main initial conditions.

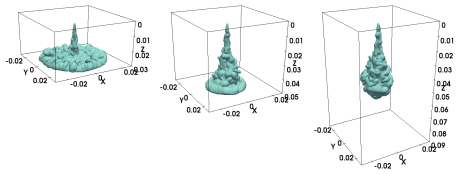

Figure 1: Configuration of the numerical cases. Sprays at 1.0 ms after the start of injection (aSOI).

Table 1: Case setup

m_f	P_{inj}	t_{inj}	T_{wall}	T_{amb}	P_{amb}
3	100	0.91	873	873	4.1
[mg]	[MPa]	[ms]	[K]	[K]	[MPa]

A fully Cartesian grid is constructed with the base cell size of 0.25 mm. The boundary layer at the wall has been refined with the final cell size of 0.083 mm. The total number of cells is 1.4, 1.8, and 2.5 million, for Case I to III, respectively. The phase space resolution in CCM is set as follows: 5K for temperature, 0.001 for the fuel mass fraction and mixture fraction, and 0.025 for the scalar dissipation rate. This phase space resolution is similar to the previously reported values [19, 20].

4. Results and discussion

4.1. Region zone structure

The reaction zone from the numerical simulations are compared with OH^* natural chemiluminescence from experiments. In the experiments, the intensity

of OH^* was recorded as line-of-sight, giving a two dimensional (2-D) distribution of the OH^* signal. To allow for a comparison, the numerical results are post-processed to obtain a numerical line-of-sight distribution by volumetric integration of a selected variable along the line-of-sight direction. Since the chemical kinetic mechanism lacks the information of OH^*, the product, OH $\times$ CO, is chosen to compare with the experimental OH^*, following the suggestion of Refs. [21, 22]. Figure 2 shows that the reaction zones, indicated by the line-of-sight integration of OH $\times$ CO predicted in the LES, is in a fairly good agreement with the experimental line-of-sight OH^*. The 50 mm wall jet case shows the strongest intensity of the OH^* signal among the three studied cases, whereas the 30 mm wall jet case shows the weakest intensity of the OH^* signal among the three cases. This trend is correctly captured in the LES.

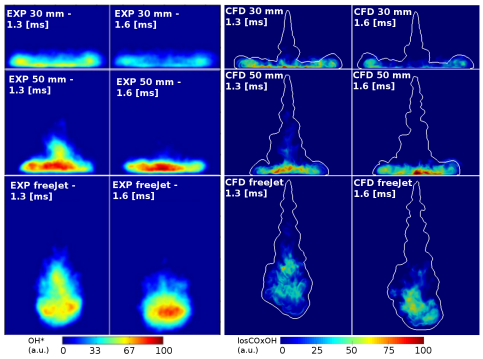

Figure 2: Comparison of experimental line-of-sight OH^* chemiluminescence [10, 11] (left columns) and simulated line-of-sight OH $\times$ CO from LES (right columns) at 1.3 ms and 1.6 ms aSOI. The white line indicates Z=0.01.

As indicated by the vapor boundary iso-line (the white line in Fig. 2), the vapor distribution in the wall jet cases can be divided into four regions [8]: the free jet region (far away from the wall), the impingement region (around the stagnation

point), the main wall jet region, and the wall jet vortex region (the furthermost vapor radial penetration region). The reaction zone is in the last three regions. The location of reaction zone predicted in the LES is in good agreement with the experiment.

4.2. Fuel consumption and oxidation

To investigate the effect of wall impingement on the combustion process, the total masses of the unburned n-dodecane vapor, $C_{12}H_{26}$, and CO in the combustion chamber are computed from the LES data. Figure 3 shows that the spray evaporation starts shortly after the start of injection at a constant rate until the time point of 0.35 ms, which corresponds to the onset of high temperature ignition of the fuel/air mixture. Thereafter, the mass of $C_{12}H_{26}$ vapor fluctuates around a nearly statistically stationary level. However, the slope of the mass of $C_{12}H_{26}$ for the 30 mm case is opposite from that for the 50 mm case and the free jet case, which imply a faster mixing, and thus a faster fuel conversion. At the end of injection (EOI) at 0.91 ms a rapid decrease of the $C_{12}H_{26}$ vapor mass is shown, which approaches a low but constant value after 1.5 ms aSOI, due to the rapid decay of turbulence in the post-injection oxidation process, which slows down the mixing controlled combustion process.

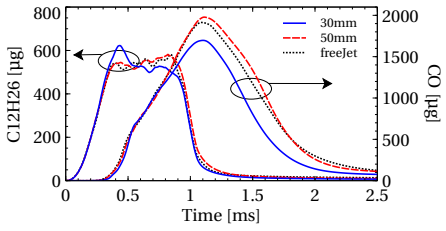

Figure 3: Mass of the unburned vapor fuel ($C_{12}H_{26}$) and CO in the domain at different time aSOI.

The CO formation starts shortly after the fuel evaporation during the low temperature ignition stage and the cool flame. The mass of CO increases rapidly after the onset of high temperature ignition, around 0.5 ms aSOI. After that, the mass of CO increases monotonically until the end of evaporation, around 1.1 ms. Thereafter, CO is oxidized in the post-injection oxidation stage in a diffusion controlled combustion mode, which slows down after 2 ms aSOI, when the turbulence is significantly decayed to a low level. The mass of the vapor fuel and CO in the 50 mm wall jet case is higher than the other two cases, specially between 0.6 ms and 1.1 ms, which is the late stage of fuel injection and evaporation. This difference will be discussed further in Section 4.4, when the air entrainment rate is analyzed.

4.3. Soot formation and oxidation

The soot formation had been analyzed in the experiment by integrating the optical thickness KL and additionally, by analyzing the 2-D distribution of KL [10, 11]. Two main observations were reported. The first is the higher slope of the integrated (KL) signal (indicating a higher soot formation rate) in the 50 mm wall jet case, which is in agreement with the higher mass of the fuel vapor and the higher mass of CO in the simulated 50 mm case, shown in Fig. 3. The second observation from the experiments is the faster decay of the integrated KL signal (thus soot) for the wall jet cases compared with the free jet case. The underlying mechanisms for soot formation/oxidation, revealed with the numerical results, will be discussed below.

The fuel conversion and CO formation is closely correlated with soot formation, suggesting the 50 mm wall jet case as the high soot formation case. Figure 4 shows a 2-D distribution of the line-of-sight optical thickness (KL) from the experiment in Refs. [10, 11], which indicates the soot region, and the equivalent

numerical line-of-sight of soot volume fraction at 1.3 ms. The LES predicted soot region is consistent with the experimentally detected KL field.

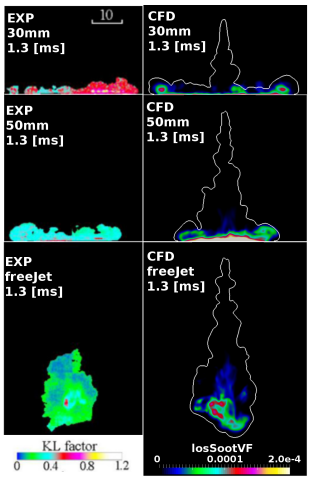

Figure 4: Line-of-sight KL signal intensity from experiments [10, 11] (left column) and an equivalent line-of-sight soot volume fraction from LES (right column).

At 1.3 ms aSOI in the 50 mm wall jet case, the peak intensity soot region is located in the impingement region, since the wall jet vortex is not sufficiently developed. The 30 mm wall jet case shows the soot region, within a thin layer in the impingement region and additionally, inside of the wall jet vortex at a moderate intensity. The free jet case shows a low intensity soot region located in the spray head, occupying a large area.

Since soot formation is essential within the mixtures of $\phi > 2$ and $1600 < T < 2200$ K, it appears that the wall jet cases can either promote or suppress the existence of such mixtures compared to the free jet case. An instantaneous temperature field with iso-lines for the $\phi = 2$, $T = 2200$ and distribution of the soot formation rate from the soot model are presented in Fig. 5 at 1.1 ms aSOI, which is prior to the time at which the integrated KL in the experiments reaches

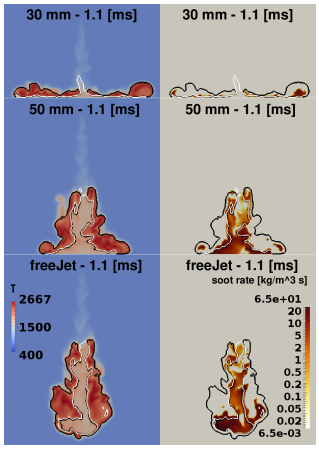

Figure 5: Numerical distribution of temperature (left column) and the modeled rate of soot formation (right column) in the center cross-section plane. White lines indicate the iso-contour of $\phi = 2$ and black lines represent the iso-contour of $T = 2200$ K.

its maximum.

In Fig. 5, the 50 mm case resulted in an accumulated zone of soot formation mixtures in the impingement region. It is partially caused by the wall cooling effect, resulting in a larger mass fraction of temperatures that correspond to the soot formation range, i.e., $1600 < T < 2200$, and in addition, since the vortex region is not yet developed, it is partially caused by the poor mixing, which gives rise to a rich mixture region, i.e., $\phi > 2$, inside of the impingement zone.

In the 30 mm wall jet case, on the other hand, even though the cooling effect is similar to that in the 50 mm wall jet case, the size of the rich fuel region, i.e., $\phi > 2$, at the impingement region, is smaller due to the faster mixing caused by the already developed wall jet vortex region. Hence, the soot formation region in the 30 mm wall jet case is reduced mainly due to the already developed vortex region, despite the wall cooling effect.

However, the largest differences in the integral of KL are observed after the

EOI. The air entrainment rate is considered as the main reason for the faster soot oxidation, and thus, it is discussed in the next section, with focus on the mixing after the EOI.

4.4. Air entrainment mechanisms

The integrated KL in the experiment of Li *et al.* [10, 11], shows a faster rate of soot oxidation for the wall jet cases compared to the free jet case. In order to explain the observed trend, including the fuel and CO analysis (Section 4.2), an air entrainment rate is calculated as the derivative of the entrained air defined as,

$$m_{ox} = (1 - Z)m_{tot}, \tag{1}$$

where m_{ox} is the entrained air, m_{tot} is the total mass of the fuel vapor, in the spray plume and Z is the mixture fraction. $Z = 0.01$ was used as a threshold to define the boundary of the spray plume. Three different air entrainment mechanisms are identified to play a role: 1) flame lift-off position, 2) wall impingement mixing, and 3) entrainment wave. The entrainment wave mixing mechanism was proposed by Musculus [13], who showed that, after EOI, as the spray jet is decelerating, the oxygen is sucked into the spray plume through the tail at a much higher speed compared to the oxygen entrainment taking place at the leading spray edge [13].

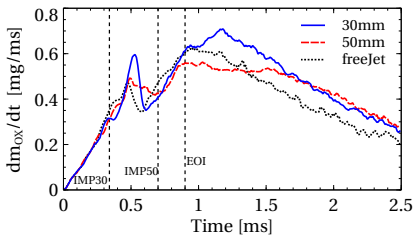

Figure 6: Air entrainment rate at different instance of time aSOI.

Figure 6 shows the rate of air entrainment and the time points of the spray impingement to the wall, for the 30 mm and the 50 mm wall jet cases, marked as IMP30 and IMP50, respectively. During the early injection stage (before IMP30), the air entrainment rate is rather similar among the three cases, since the spray plume is in the free jet region. Between IMP30 and IMP50, the 30 mm wall jet case shows a significant boost of air entrainment; the peak air entrainment rate is higher than the 50 mm wall jet case and the free jet case. The enhanced air mixing is due to the wall impingement mixing mechanism. The wall impingement enhanced the production of turbulence, which is in favor of fuel/air mixing.

After the onset of high temperature ignition (~ 0.5 ms), the air entrainment rate shows a sudden decrease for all three cases. It appears that the hot gas expansion inside the spray plume slows down the entrainment of ambient air. For the free jet case and the 30 mm wall jet case, this effect is similar and overcomes at the same time (~ 0.6 ms). The 50 mm wall jet case shows a lower, but continuous decrease of the air entrainment rate until the spray reaches the wall, i.e., at IMP50. The lower decrement of the air entrainment rate in the 50 mm wall jet case can be explained by the longer flame lift-off length compared to other two cases, Fig. 7. The longer flame lift-off length enables air entrainment in a large distance upstream the flame region, counteracting the gas expansion effect. At the EOI, the air entrainment rate is favorable for the 30 mm and free jet cases, but disadvantageous for the 50 mm case.

The faster soot oxidation for the wall jet cases, observed in the experiments, takes place after the EOI, thus the mechanisms of air entrainment during the post-injection phase are considered as the reason for the differences in the soot oxidation process. One can note that LES resulted in a significantly different air

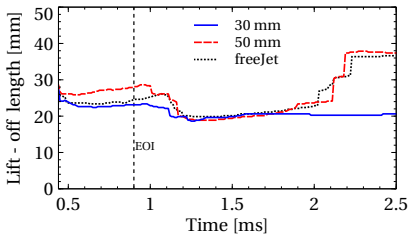

Figure 7: Lift-off length.

entrainment rate after the EOI, Fig 6. After the EOI, the air entrainment is governed by two mechanisms, the impingement enhanced mixing for the wall cases and the entrainment wave mixing for all cases.

Figure 6 shows that after the EOI, the rate of the air entrainment for the 50 mm wall jet case is lower than in the other two cases, but it stays at a constant level, forming a "mixing plateau" between EOI and 1.7 ms aSOI. For the 30 mm case, air entrainment resulted in the highest peak of air entrainment rate forming a "mixing boost". The free jet case, resulted in a constant decay of the air entrainment starting from the EOI. To understand this behavior, the temporal evolution of the oxygen mass fraction is examined for the post-injection combustion stage, Fig. 8.

At 1 ms aSOI, which is a time point shortly after EOI, a large dark region can be seen in all cases, Fig. 8, which is the region of the fuel rich combustion zone where oxygen has been completely consumed. The region is filled with unburned fuel, CO, and soot, along with other combustion products and intermediate species. The oxygen depleted dark region becomes smaller with time, due to the impingement mixing and entrainment wave mixing during the post-injection oxidation process. The importance of those two air mixing mechanisms can be identified, by analyzing the direction from which the oxygen front is moving into

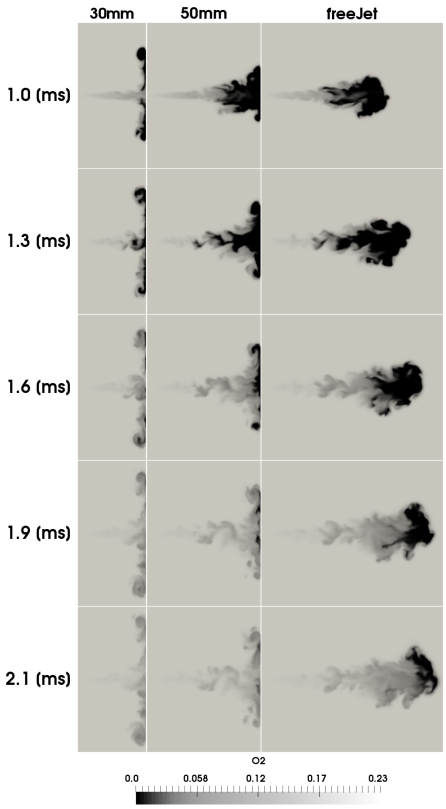

Figure 8: Distribution of O_2 mass fraction at different time aSOI.

the low oxygen region.

In the 50 mm wall jet case, from 1 ms to 1.6 ms aSOI, the entrainment wave mechanism is the governing one, since the oxygen front is propagating from the tail of the free jet region towards the wall. After 1.6 ms aSOI, the wall impingement mechanism is the dominant one, since the air mixing is mainly in the impingement region and the wall jet region, as a consequence of late vortex mixing. These two mechanisms work sequentially in time, which results in the "mixing plateau" shown in Fig. 6.

In the 30 mm wall jet case, the oxygen front penetrates into the impingement

region, the wall jet region and the wall jet vortex region at an equal rate. Thus, in this case, the main mixing mechanism is the wall impingement enhanced mixing [12], supported by the entrainment wave. The air entrainment rate of the 30 mm wall jet case reaches its highest peak after EOI, ($\sim$ 1.2 ms), cf. Fig. 6. Due to the strongest spray-wall interaction, with a well developed main wall jet region and the wall jet vortex region, the fuel rich region is located in the thin wall jet boundary layer, where rapid mixing takes place, leading to "mixing boost".

In the free jet case, the oxygen front propagates from the tail of the spray into the head of the spray, due to the slowing down of the spray head after EOI, which indicates that the governing mechanism is the entrainment wave mechanism [13]. Since there is no impingement enhanced mixing, the mixing in the leading spray head region is mainly due to the local turbulent structures, which is much weaker compared to impingement enhanced mixing, as indicated by the sharp gradient of oxygen in the spray head region. The peak air entrainment rate for the free jet case is at EOI, cf. Fig. 6, and it starts to decay just after the EOI, giving rise to a lower air entrainment.

At the later times, i.e., from 1.9 ms to 2.1 ms aSOI, the low oxygen concentration region in the free jet case is the largest, while the two wall jet cases show almost complete oxidation of the fuel, CO and soot in the spray plume. Hence, it is clear that the slower oxidation rate of soot in the free jet case is correlated with the slower air entrainment, where it takes a longer time for the oxygen front to penetrate into the remaining soot region, located in the spray head.

The mixing rate shown in Fig. 6 indicates that the free jet case has the lowest air entrainment in total. The two wall jet cases have higher air entrainment rate, however, due to a different mixing sequence. The 50 mm wall jet case resulted in

a "mixing plateau" that maintained the mixing rate at a constant rate, due to the two air entrainment mechanisms working in sequence. The 30 mm wall jet case resulted in a "mixing boost", due to the strongest spray-wall interaction, which maximized the air entrainment rate just after the EOI. Thus, compared with the free jet case, the faster oxidation of soot in the 30 mm wall jet case is caused by the "mixing boost", whereas in the 50 mm wall jet case, the faster oxidation of soot is caused by the "mixing plateau". The above described mixing mechanisms correlate strongly with the decay rate of the integral of the experimental KL in Refs. [10, 11].

5. Conclusions

An LES study of diesel spray-wall interaction was carried out. Two different wall positions, with a 30 mm and 50 mm nozzle-to-wall distance, were studied and compared with the free jet case. It was found that the formation of soot during the injection phase, prior to the enhanced mixing by the impingement wall jet vortex, could be promoted due to the presence of the wall, where the local mixture composition is in favor of the soot formation. The region of high soot formation can be reduced if the wall distance is short enough to create strong impingement enhanced mixing due to the impingement vortex, at the time of the soot formation.

The main finding is the different air entrainment mechanisms that govern the oxidation process after the EOI. The experimental KL implies that the oxidation of soot is faster for both wall jet cases compared to the free jet case. LES results revealed that the reason behind the faster oxidation of soot in 30 mm and 50 mm wall jet cases is different. The air entrainment in the 30 mm wall jet case is caused

by the "mixing boost", where impingement enhanced mixing is strongest due to the developed wall jet region and the wall jet vortex region. The air entrainment in the 50 mm wall jet case is caused by the "mixing plateau", where impingement enhanced mixing and entrainment wave mixing act in a sequence and maintains a constant air entrainment rate. The free jet case relies on the entrainment wave mixing mechanism. As a result, the air mixing into the spray plume is the slowest, which results in the slowest oxidation rate of soot among the three studied cases.

6. Acknowledgments

This work is sponsored by Swedish Energy Agency and Competence Center for Combustion Processes (KCFP). The simulations were performed on resources provided by the Swedish National Infrastructure for Computing (SNIC) at PDC and HPC2N centers.

7. References

[1] L. Rao, Y. Zhang, S. Kook, K. S. Kim, C. B. Kweon. Understanding in-cylinder soot reduction in the use of high pressure fuel injection in a small-bore diesel engine, Proc. Combust. Inst. 37 (2019) 4839–4846.

[2] K. Al-Qurashi, A. L. Boehman. Impact of exhaust gas recirculation (EGR) on the oxidative reactivity of diesel engine soot, Combust. Flame 155 (2008) 675–695.

[3] A. Hadadpour, M. Jangi, X. S. Bai. Jet-jet interaction in multiple injections: A large-eddy simulation study, Fuel 234 (2018) 286–295.

[4] G. Bruneaux. Mixing process in high pressure diesel jets by normalized laser induced exciplex fluorescence part I: Free jet, SAE Tech. Pap. c (2005).

[5] G. Bruneaux. Combustion structure of free and wall-impinging diesel jets by simultaneous laser-induced fluorescence of formaldehyde, poly-aromatic hydrocarbons, and hydroxides, Int. J. Engine Res. 9 (2008) 249–265.

[6] N. Maes, The life of a spray, 2019.

[7] S. Skeen, K. Yasutomi, E. Cenker, B. Adamson, N. Hansen, L. Pickett. Standardized Optical Constants for Soot Quantification in High-Pressure Sprays, SAE Int. J. Engines 11 (2018) 805–816.

[8] L. M. Pickett, J. J. López. Jet-wall interaction effects on diesel combustion and soot formation, SAE Tech. Pap. 2005 (2005).

[9] X. Wang, Z. Huang, W. Zhang, O. A. Kuti, K. Nishida. Effects of ultra-high injection pressure and micro-hole nozzle on flame structure and soot formation of impinging diesel spray, Appl. Energy 88 (2011) 1620–1628.

[10] K. Li, P. Dong, T. Matsuo, B. Shi, Y. Ogata, K. Nishida. Characteristics of Diesel Spray Flame under Flat Wall Impinging Condition –LAS, OH* Chemiluminescence and Two Color Pyrometry Results, SAE Tech. Pap. Ser. 1 (2014).

[11] K. Li, M. Ido, Y. Ogata, K. Nishida, B. Shi, D. Shimo, Effect of Spray/Wall Interaction on Diesel Combustion and Soot Formation in Two-Dimensional Piston Cavity, Technical Report, 2013.

[12] G. Bruneaux, M. Causse, A. Omrane. Air entrainment in Diesel-like gas jet by simultaneous flow velocity and fuel concentration measurements, comparison of free and wall impinging jet configurations, SAE Int. J. Engines 5 (2012) 76–93.

[13] M. P. Musculus. Entrainment waves in decelerating transient turbulent jets, J. Fluid Mech. 638 (2009) 117–140.

[14] K. M. Pang, M. Jangi, X. S. Bai, J. Schramm. Investigation of chemical kinetics on soot formation event of n-Heptane spray combustion, SAE Tech. Pap. 1 (2014).

[15] C. Gong, M. Jangi, T. Lucchini, G. D'Errico, X. S. Bai. Large eddy simulation of air entrainment and mixing in reacting and non-reacting diesel sprays, Flow, Turbul. Combust. 93 (2014) 385–404.

[16] T. Yao, Y. Pei, B.-J. Zhong, S. Som, T. Lu. A Hybrid Mechanism for n-Dodecane Combustion with Optimized Low-Temperature Chemistry, 9th U. S. Natl. Combust. Meet. (2015) 1–10.

[17] T. Yao, Y. Pei, B. J. Zhong, S. Som, T. Lu, K. H. Luo. A compact skeletal mechanism for n-dodecane with optimized semi-global low-temperature chemistry for diesel engine simulations, Fuel 191 (2017) 339–349.

[18] J. Chomiak, A. Karlsson. Flame liftoff in diesel sprays, Symp. Combust. 26 (1996) 2557–2564.

[19] M. Jangi, R. Yu, X. S. Bai. A multi-zone chemistry mapping approach for direct numerical simulation of auto-ignition and flame propagation in a constant volume enclosure, Combust. Theory Model. 16 (2012) 221–249.

[20] M. Jangi, X. S. Bai. Multidimensional chemistry coordinate mapping approach for combustion modelling with finite-rate chemistry, Combust. Theory Model. 16 (2012) 1109–1132.

[21] J. E. Rehm, P. H. Paul. Reaction rate imaging, Proc. Combust. Inst. 28 (2000) 1775–1782.

[22] J. H. Frank, S. A. Kaiser, M. B. Long. Reaction-rate, mixture-fraction, and temperature imaging in turbulent methane/air jet flames, Proc. Combust. Inst. 29 (2002) 2687–2694.